Zhu *et al. PhotoniX* (2024) 5:34
https://doi.org/10.1186/s43074-024-00149-0

PhotoniX

RESEARCH Open Access

Three-dimensional computer holography with phase space tailoring

Runze Zhu[1†], Lizhi Chen[1†], Jiasheng Xiao[1] and Hao Zhang[1*]

[†]Runze Zhu and Lizhi Chen contributed equally to this work.

*Correspondence: haozhang274@tsinghua.edu.cn

[1] Department of Precision Instrument, State Key Laboratory of Precision Measurement Technology and Instruments, Tsinghua University, Beijing 100084, China

Abstract

Computer holography is a prominent technique for reconstructing customized three-dimensional (3D) diffraction fields. However, the quality of optical reconstruction remains a fundamental challenge in 3D computer holography, especially for the 3D diffraction fields with physically continuous and extensive depth range. Here, we propose a 3D computer-generated hologram (CGH) optimization framework with phase space tailoring. Based on phase space analysis of the space and frequency properties in both lateral and axial directions, the intensity of the 3D diffraction field is adequately sampled across a large depth range. This sampling ensures the reconstructed intensity distribution to be comprehensively constrained with physical consistency. A physics-informed loss function is constructed based on the phase space tailoring to optimize the CGH with suppression of vortex stagnation. Numerical and optical experiments demonstrate the proposed method significantly enhances the 3D optical reconstructions with suppressed speckle noise across a continuous and extensive depth range.

Keywords: Computer-generated holograms, Spatial light modulation, Three-dimensional display, Phase space optics

Introduction

Computer holography enables the reconstruction of arbitrary wavefront using a single synthesized hologram, making it a versatile technology with applications in micro fabrication [1], neural photo-stimulation [2, 3], optical tweezers [4, 5], and 3D display [6–11]. With advancements in spatial light modulators (SLMs), computer-generated holograms (CGHs) can be dynamically reconstructed through phase or amplitude modulation. Phase holograms, in particular, are extensively investigated due to their high diffraction efficiency and absence of conjugate images, which allows a better utilization of the space-bandwidth product (SBP) [12]. However, the encoding process of phase holograms always introduces speckle noise and artifacts during optical reconstruction, leading to image degradation. As a result, synthesizing CGHs to achieve high-quality 3D images with a continuous and large depth range remains a significant challenge.

One straightforward approach to generate phase holograms is preserving the phase components of complex-valued fields. Typically, a random phase is used to diffuse the object wave [13], which always results in severe speckle noise during optical reconstruction due to the random walk phenomenon of coherent light [14–16]. Another

direct technique, known as the double phase method, decomposes a complex amplitude hologram into the superposition of two phase holograms [17, 18], aiming to reduce the speckle noise in optical reconstruction [19, 20]. However, the interlacement of the decomposed phase holograms would impair the effective utilization of the SLMs' space-bandwidth product. Furthermore, the coding error arising from the spatial displacement of decomposed phase values further degrades the image quality and diffraction efficiency during optical reconstruction.

Compared with direct methods, optimization methods for generating phase holograms can effectively suppress speckles and artifacts through an iterative process. The classic optimization methods include the Gerchberg-Saxton (GS) algorithm and its modified versions [21–23]. These methods usually yield inconsistent results between simulations and optical experiments, primarily due to the limitations of discrete wave propagation models. Inadequate modeling of wave propagation has a more pronounced effect on iterative methods compared to the direct methods. This is because the iterative optimization requires multiple diffraction calculations, and the modeling errors will accumulate over time. Band-limited angular spectrum method (ASM) [24] is a fundamental work that concerns the sampling problem of diffraction calculation. This method corrects the sampling of the transfer function in the far field, allowing for an accurate sampling of complex amplitude fields. However, accurately sampling the intensity field remains challenging, and this limitation significantly affects the performance of iterative optimization methods. The state-of-the-art optimization methods, such as the bandwidth constraint method [25] and the hardware feedback method (camera-in-the-loop, CITL), have demonstrated the ability to achieve superior two-dimensional (2D) images during optical reconstructions [26–28]. The effectiveness of the bandwidth constraint method stems from its use of a diffraction model consistent with optical reconstruction. Go one step further, the CITL method directly replaces the diffraction model with an optical reconstruction. However, the lack of a comprehensive space-frequency analysis of 3D diffraction fields still hampers these optimization methods from achieving high-quality 3D optical reconstructions with a continuous and large depth range.

The compression of three-dimensional spatial properties into a flat optical element poses a highly ill-posed and non-convex problem. Several methods have been developed to address this challenge. For instance, Non-Convex Optimization for VOlumetric CGH (NOVO-CGH) utilizes a non-convex optimization strategy that effectively resolves the crosstalk issues in 3D diffraction fields [29]. An alternative approach combines stochastic gradient descent (SGD) with a complex loss function, enabling the efficient design of 3D CGHs [30]. By leveraging the orthogonality of random vectors, crosstalk-free reconstructions across multi-layers can be achieved [31]. As with 2D cases, an appropriate diffraction model is essential for accurately sampling the diffraction fields during discrete calculations. Nevertheless, in these methods, the diffraction model and sampling strategies were not adequately designed to account for the bandwidth properties of the diffraction fields. As a result, there is a violation of Nyquist's sampling theorem throughout the optimization, leading to the degraded optical results. In contrast, the 3D CITL method, assisted by neural networks, has achieved noiseless 3D optical reconstructions at 8 discrete depths [32]. This technology has also been developed to combine with metasurface waveguides [33]. Nonetheless, the hardware used in this approach has

fixed sampling parameters, which fails to account for the varying bandwidth properties of 3D diffraction fields at different depths, ultimately limiting the depth range and causing discontinuities. Another approach involves time-multiplexed CGHs with focal stack supervision, which can produce photorealistic 3D optical reconstructions [34, 35]. However, this method typically requires high frame-rate SLMs. Recently, with advancements in deep learning, it has proven to be efficient in various optical applications, including computational imaging [36, 37] and computational displays [38]. In the field of computer holography, deep learning offers an effective balance between the computation speed and the quality of reconstructed images [20, 39]. For deep learning-based CGH, the diffraction model remains crucial, whether it is used to generate datasets [39] or as a physical prior [40].

To effectively optimize the 3D diffraction fields in computer holography, a comprehensive bandwidth analysis is essential. This analysis facilitates the establishment of a forward diffraction model with physically consistent sampling. The phase space, which combines both space and spatial frequency into a unified coordinate system, serves as a powerful tool for analyzing the evolution of the SBP during wave propagation [41–44]. By simultaneously considering both space and frequency domains, the bandwidth properties of the 3D diffraction fields can be thoroughly analyzed. This insights then enables the development of an efficient discrete calculation model for synthesizing the forward diffraction process under various parameters [43, 44].

In this study, we propose a generalized framework for optimizing CGH using phase space tailoring. This framework aims to comprehensively constrain the discrete sampling of the 3D diffraction fields. To achieve this, the lateral and axial bandwidth properties are analyzed in the phase space domain. Then the phase space tailoring technique is applied to the discrete diffraction model, enabling the effective intensity sampling of the 3D diffraction fields across all depths. During the optimization process, a physics-informed loss function comprehensively constraints the intensity and phase distributions, incorporating the phase space tailoring implementation. This approach enables an efficient optimization process while solving the vortex stagnation problem caused by the phase singularities in the diffraction fields. Furthermore, the phase space tailoring technique significantly reduces the sampling requirement in 3D space, making it effective for optimizing diffractive fields with a continuous and large depth range. Theoretical analysis and optical experiments demonstrate that the proposed CGH optimization framework can achieve high-quality speckle-free 3D optical reconstructions with a continuous and extensive depth range.

Results

Phase-space analysis for 3D CGH reconstruction

In 3D computer holography, the modulated wavefront $U(u,v)$ from the CGH diffracts in free space to reconstruct the 3D diffraction field $O(x,y,z)$. During the reconstruction, the ASM is implemented for diffraction calculation without paraxial approximation:

$$O(x,y,z) = \mathrm{IFT}\left\{\mathrm{FT}\{U(u,v)\}H^{(z)}\right\}, \tag{1}$$

where FT and IFT denote the Fourier transform and the inverse Fourier transform, respectively. $H^{(z)}$ is the transfer function under the propagation distance z and expressed as:

$$H^{(z)}(f_x,f_y)=\begin{cases}\exp\left(\mathrm{i}\frac{2\pi}{\lambda}z\sqrt{1-(\lambda f_x)^2-(\lambda f_y)^2}\right) & ,if\ \sqrt{f_x^2+f_y^2}<\frac{1}{\lambda}\\ 0 & ,otherwise\end{cases}, \tag{2}$$

where (f_x,f_y) are spatial frequencies, i is the imaginary unit, λ is the wavelength.

Before analyzing the phase space evolution of the diffraction fields, we first introduce an upgrading dimension analysis tool known as the Wigner distribution function (WDF). The WDF is a useful tool for describing space-frequency relationships. It was initially developed in quantum mechanics and later introduced into the optical community [45, 46]. For a one-dimensional complex amplitude field $O(x)$, the WDF is defined as:

$$W(x,f_x)=\int O\left(x+\frac{x'}{2}\right)O^*\left(x-\frac{x'}{2}\right)exp(-\mathrm{i}2\pi x'f_x)dx', \tag{3}$$

where $W(x, f_x)$ is the WDF, x is the spatial coordinate, f_x is the spatial frequency coordinate, and * denotes the complex conjugate. The phase space diagram (PSD) represents the domain where the WDF values are significantly non-zero. In this study, the PSD is used to describe the phase space characteristics of the diffraction fields. Figure 1 illustrates the PSDs for both the complex amplitude and intensity of the diffraction fields. In these diagrams, the horizontal axis denotes the spatial position, while the vertical axis denotes the local spectrum of the spatial frequency at that particular spatial position.

The spectrum of complex field is obtained by projecting the WDF along the space direction:

$$\left|\hat{O}(f_x)\right|^2=\int W(x,f_x)dx, \tag{4}$$

where $\hat{O}(f_x)$ is the Fourier transform of $O(x)$. According to this relationship, the spatial frequency bandwidth of $O(x)$ corresponds to the extent of the PSD along the spatial frequency axis. Additionally, the local bandwidth refers to the extent of the vertical section of the PSD at a particular spatial position, as indicated by the white double-arrow lines in Fig. 1b and c. As a result, the sampling criteria that comply with the Nyquist's sampling theorem can be determined by considering the bandwidth characteristics of the diffraction fields.

The phase space of the input field $U(u)$, which has a lateral spatial extent L_U and bandwidth B_U, undergoes the shear deformation during diffraction. The magnitude of this shear deformation, as well as the local bandwidth of the diffraction field, depend on the propagation distance (Fig. 1b). It is important to note that the WDF of the intensity field is the autocorrelation of the WDF of the complex amplitude field. Consequently, the local bandwidth of the intensity field is twice that of the complex amplitude field (Fig. 1c). Additionally, the WDF of the intensity field along the axial direction can be

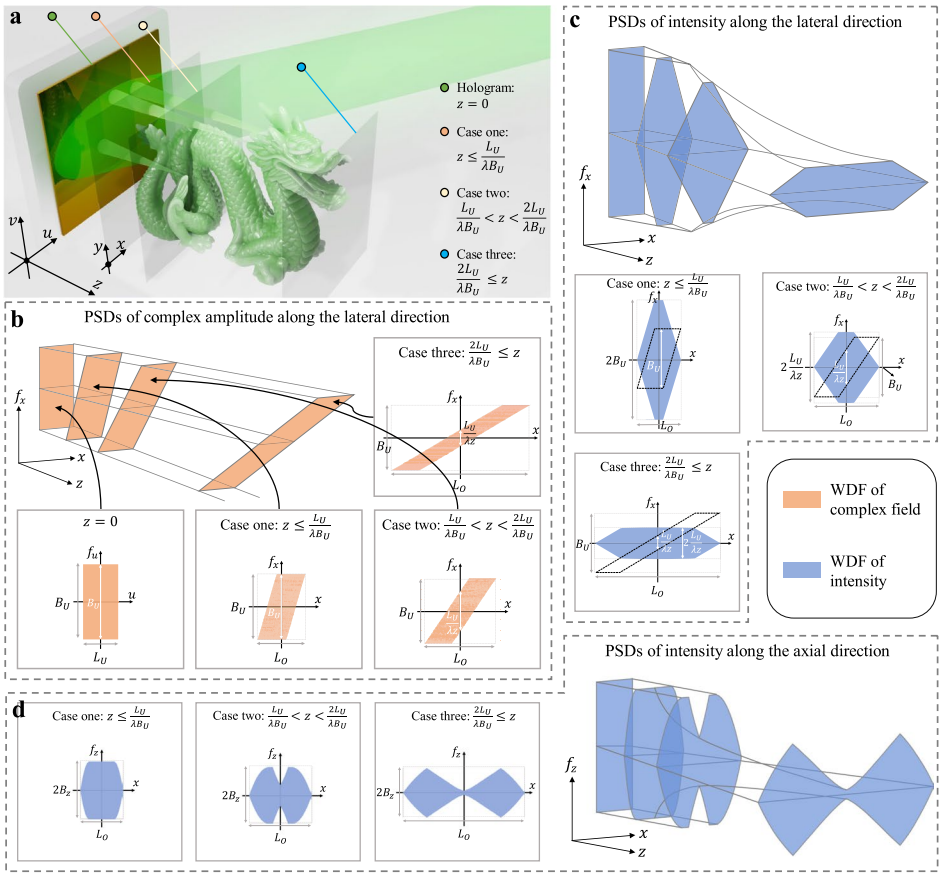

Fig. 1 Phase space transformation during diffraction. **a** Sketch of 3D computerholography. **b** Phase space transformation of the complex amplitude with input field $U(u)$, spatial extent L_U, and bandwidth B_U along the lateral direction. **c** Phase space transformation of the intensity along the lateral direction. **d** Phase space transformation of the intensity along the axial direction

derived using the same analysis (Fig. 1d). In summary, the global bandwidth of the intensity field is always twice the maximum local bandwidth of the corresponding complex amplitude field, which varies with the propagation distance z. For a more detailed description of phase-space analysis for 3D CGH, please refer to Sect. 1A and Sect. 1B of the Supplementary Materials. Interested readers may also find the papers about sampling analysis of numerical diffraction [42, 43] helpful.

Phase space tailoring

According to the phase space analysis of the reconstructed diffraction fields, we design a numerical diffraction model with appropriate sampling, which improves the alignment of the wave propagation model with the physical one. The key to this model is the phase space tailoring, which reshapes the PSDs of reconstructed intensity fields.

In the ASM implemented with the fast Fourier transform algorithm, the sampling interval d_x of the output fields is the same as that of the input fields. Thus, the sampling frequency of the intensity fields on the image plane is $1/d_x$. To ensure accurate sampling without aliasing, the maximum allowable spatial frequency of the intensity fields

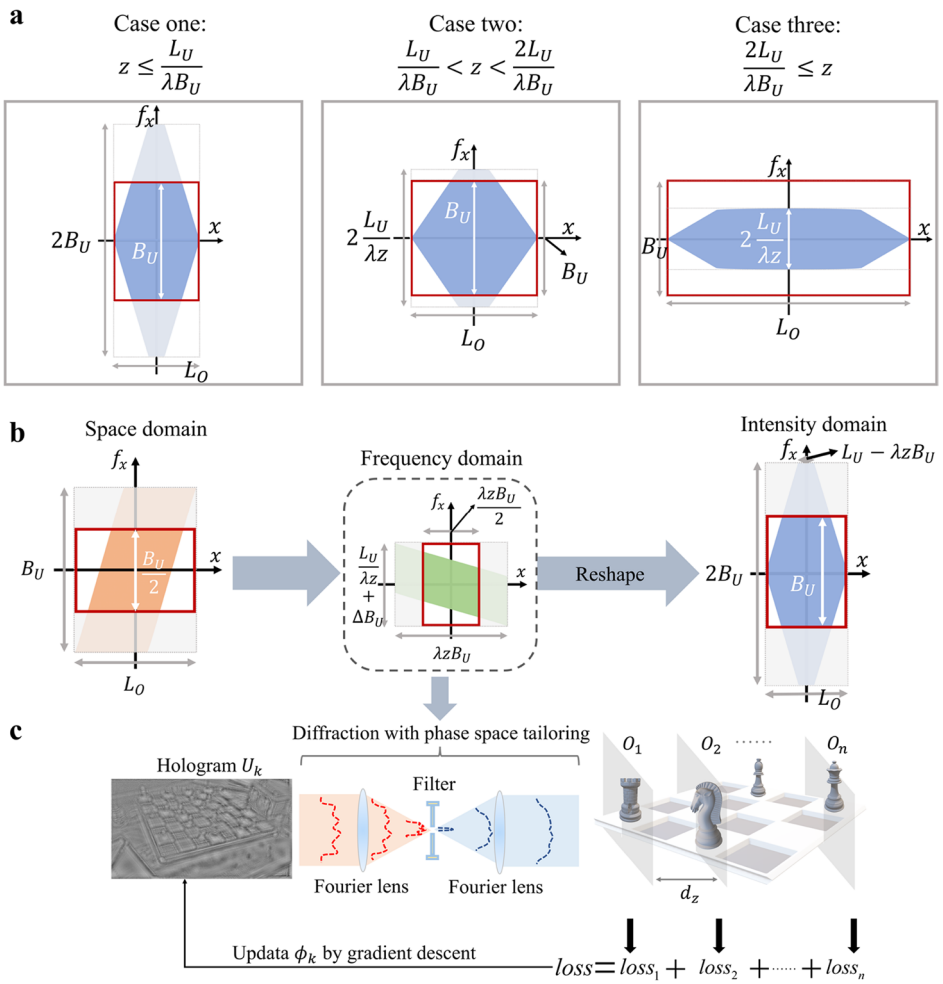

Fig. 2 CGH optimization with phase space tailoring. **a** PSDs of inaccurate sampling. The signal outside the red rectangle would cause aliasing, and is tailored along the spatial frequency axis. **b** Phase space tailoring in space domain, frequency domain, and intensity domain. **c** Schematic diagram for CGH optimization, the loss functions calculated with the reconstructed intensity at different depths are summed and then used to optimize the phase hologram by the gradient descent method

is $1/(2d_x)$, which is equal to half of the input field bandwidth $B_U/2$. In Fig. 2a, the red rectangle represents the range of frequency components that can be accurately sampled in numerical calculations. However, the speckle noise and artifacts with high-frequency components fall outside this range, as depicted with light-gray area (Fig. 2a). Therefore, the original ASM fails to effectively depict the reconstructed intensity fields. The bandwidth property in the axial direction can be analyzed similarly. For a more detailed analysis, please refer to Sect. 1C of the Supplementary Materials.

To correctly sample the intensity fields, an effective approach is to tailor the PSDs of the complex amplitude fields. This reshapes the PSDs of the intensity fields and ensures that they satisfy Nyquist's sampling theorem. Figure 2b illustrates that by clipping the WDF of the complex amplitude fields that exceeds $B_U/2$ along the spatial frequency axis, the bandwidth of the intensity fields will be confined to the correct sampling range. Direct frequency tailoring of the phase space along the spatial frequency axis is not

feasible in the space domain. However, in the Fourier domain, the frequency tailoring is transformed into spatial tailoring, which can be achieved easily through the spatial filtering (Fig. 2b). The diameter of the filter increases with the propagation distance and is given by $A_x = \lambda z/2d_x$. The modified ASM is then reformulated as:

$$O(x,y,z) = \mathrm{IFT}\left\{S^{(z)}\left\{\mathrm{FT}\{U\}H^{(z)}\right\}\right\} = P_{PST}^{(z)}\{U\}, \tag{5}$$

where $S^{(z)}$ represents the frequency filtering operation and $P_{PST}^{(z)}$ represents the operator of the proposed phase space tailoring technique under the propagation distance of z. The variational filter diameter, A_x, can be easily handled in simulations, the Fast Fourier Transform algorithm transforms the input field into its frequency domain, allowing for the filtering of the information outside the range determined by A_x. In the optical experiments, a $4f$ system is necessary to perform the Fourier transform and the frequency filtering. In this implementation, the filtering operation is conducted in k-space, the diameter of the filter for all diffraction distances is determined according to the focal length of the Fourier transform lens (Fig. 2c). Therefore, $S^{(z)}$ and A_x can be defined as follows:

$$S^{(z)} = \begin{cases} 1 & \left(\lambda z f_x\right)^2 + \left(\lambda z f_y\right)^2 \le A_x^2/4 \\ 0 & \text{else} \end{cases}, \quad A_x = \begin{cases} \lambda z/2d_x & \text{in free space (simulation)} \\ \lambda z_f/2d_x & \text{in } 4f \text{ system (optical)} \end{cases} \tag{6}$$

where z_f is the focal length of the Fourier transform lens in $4f$ system. As the $4f$ filtering is completed before the free space diffraction, the optimal diameter of the filter remains constant for each z location of the 3D volume. And there is no requirement to dynamically adjust the diameter of the filter for different z location. This property makes the phase space tailoring technique both convenient and practical for implementation in practice. Please refer to Sect. 2D of the Supplementary Materials for a more detailed discussion about the $4f$ system filtering. And see Sect. 1D and Sect. 2A of the Supplementary Materials for a more detailed discussion about the differences between the proposed phase space tailoring and the previous band-limited ASM [24].

CGH optimization with phase space tailoring

The phase space tailoring ensures that the intensity is adequately sampled, enhancing the consistency between the numerical diffraction calculation model and the physical one. However, simply tailoring the phase space without further optimization leads to the degraded image quality of the CGHs due to information loss. To achieve high-quality 3D optical reconstructions, the further optimization is essential. This optimization process helps to redistribute the information of the reconstructed images into the tailored PSD.

The gradient descent method is used to solve the following loss function:

$$\arg\min_{U} \; loss = loss_I + \lambda_{Per} loss_{Per} + \lambda_{Vor} loss_{Vor} + \lambda_W loss_W, \tag{7}$$

where U is the hologram, $loss_I$ and $loss_{Per}$ are the data matching terms which measure the difference between the reconstructed intensity and the target intensity. $loss_I$ is the mean square error, while $loss_{Per}$ is a perception-informed SSIM regularization term. In most cases, the speckle noise in the reconstructed images is caused by the phase singularities, also known as the phase vortices. These phase singularities are difficult to be removed using only the intensity constraints $loss_I$ and $loss_{Per}$ [47–49] (Fig. 6b, c). Therefore, to improve the performance of the optimization algorithm, a vortex regularization term $loss_{Vor}$ is developed according to the physical structure of phase vortex. $loss_{Vor}$ accounts for the phase vortices through a specially designed stochastic phase gradient approach. To broaden the optimization space and enhance the reconstructed image contrast, a modified weighted constraint strategy is implemented (see Methods and Sect. 2G of the Supplementary Materials for the details of this method). This strategy assigns different weights to the regularization terms $loss_{Vor}$ and a masked intensity constraint term $loss_W$ according to the image contents [50]. λ_{Vor}, λ_{Per} and λ_W are the weights of the regularization terms. The calculation time consumption for each loss term can be found in Sect. 2F of the Supplementary Materials.

With a stochastic gradient descent-based optimizer like Adam, the loss function can be used to optimize the CGH efficiently. Additionally, this CGH optimization algorithm can be naturally combined with layer-oriented method to design the 3D CGHs [14, 51]. In the layer-oriented method (Fig. 2c), a 3D scene is divided into N depth layers according to the depth map $D(x,y)$, where O_i represents the ith depth layer ($i=1,...,N$). Each depth layer contains amplitude information within a specific depth range, which can be calculated using $O_i = M_i P_{PST}^{(zi)}\{U\}$. M_i is a binary mask defined as:

$$M_i(x,y) = \begin{cases} 1 & z_1 + (i-1)d_z \le D(x,y) \le z_1 + id_z, \quad i = 1,...,N-1 \\ 0 & \text{otherwise} \end{cases}, \tag{8}$$

where z_1 is the distance between the CGH and the first depth layer, d_z is the distance between adjacent depth layers. Thus, the loss function for 3D CGH optimization is written as:

$$\begin{aligned} loss = & \sum_{i=1}^{N} \| s|O_i| - M_i T \|_2 \\ & + \sum_{i=1}^{N} \lambda_{Per}(1 - SSIM\{s|O_i|, M_i T\}) \\ & + \sum_{i=1}^{N} \lambda_{Vor} loss_{Vor}\left\{P_{PST}^{(z_i)}\{U\}, M_i\right\} \\ & + \sum_{i=1}^{N} \lambda_W loss_W\{s|O_i|, T\}, \end{aligned} \tag{9}$$

where T is the target image and N is the number of depth layers. The learnable scale factor s takes into account the difference between the total energy of reconstructed intensity and target image, which helps to accelerate the convergence of the algorithm.

As an optimization-based CGH design method, an appropriate forward model is crucial to ensure the consistency of the reconstructions in numerical simulations and optical experiments. In the proposed method, the optimization process incorporates a forward propagation model with phase space tailoring. Benefiting from the appropriate sampling strategy of the diffraction fields, any destructive aliasing during the optimization process is avoided. Building upon the aforementioned forward model, a physics-informed loss function is designed to comprehensively constrain the 3D diffraction fields.

Experimental verification

The feasibility of the proposed phase space tailoring method is validated through simulations and optical experiments. The proposed method is compared to a modified state-of-the-art GS method [23, 25, 50], double phase method [19], and original SGD method [27]. In order to evaluate the quality of the reconstructed images, peak signal-to-noise ratio (PSNR), structural similarity index measure (SSIM), and speckle contrast (SC) are used. The test images are selected from the DIV2K dataset [52, 53]. The PSNR and SSIM evaluate the overall quality of the images, with higher values indicating better image quality. On the other hand, the SC reflects the local roughness of the images and lower values indicate less local noise. To ensure the consistency with the optical experiments, a modified sampling method is employed in the comparisons [25]. The simulation results presented here (Fig. 3c), using the modified sampling method, may not match the quality of those in previous works [27]. However, they are more consistent with the optical results. The simulation results for 2D images (Fig. 3b) and quantitative comparisons (Fig. 3c) demonstrate that the proposed method outperforms other methods in terms of image quality.

The superior performance of the phase space tailoring method is demonstrated with optical experiments. Figure 3d shows the full-color 2D results, while Table S2 in the Supplementary Materials presents an evaluation of the proposed method compared to existing methods using more data. Both the GS and SGD methods produce results with significant speckle noise. Although the double phase method performs slightly better, it still introduces artifacts in the reconstructed images, as shown in the enlarged images. In contrast, the phase space tailoring method achieves the highest image quality, successfully eliminating speckle noise and artifacts. The quantitative evaluations, located at the top right of each image, confirm that the proposed method achieves the highest PSNR and SSIM along with the lowest SC. Additionally, our proposed method provides better color fidelity in the optical reconstructions. For a more detailed analysis about the color fidelity of the optical results, please refer to Sect. 2E of the Supplementary Materials.

The proposed method is further evaluated for holographic multi-plane reconstruction. The optical reconstructions of three 2D images placed at different depths are presented in Fig. 4a. From the first row to last row of the enlarged images, the focus shifts from the near plane to the middle plane, and finally to the far plane. The enlarged images clearly illustrate the in-focus and out-of-focus effects. Compared to the 2D cases, the speckles and artifacts in the first three algorithms are more severe. The phase space tailoring method effectively handles this type of 3D images, yielding the optical reconstructions with the highest overall quality and contrast.

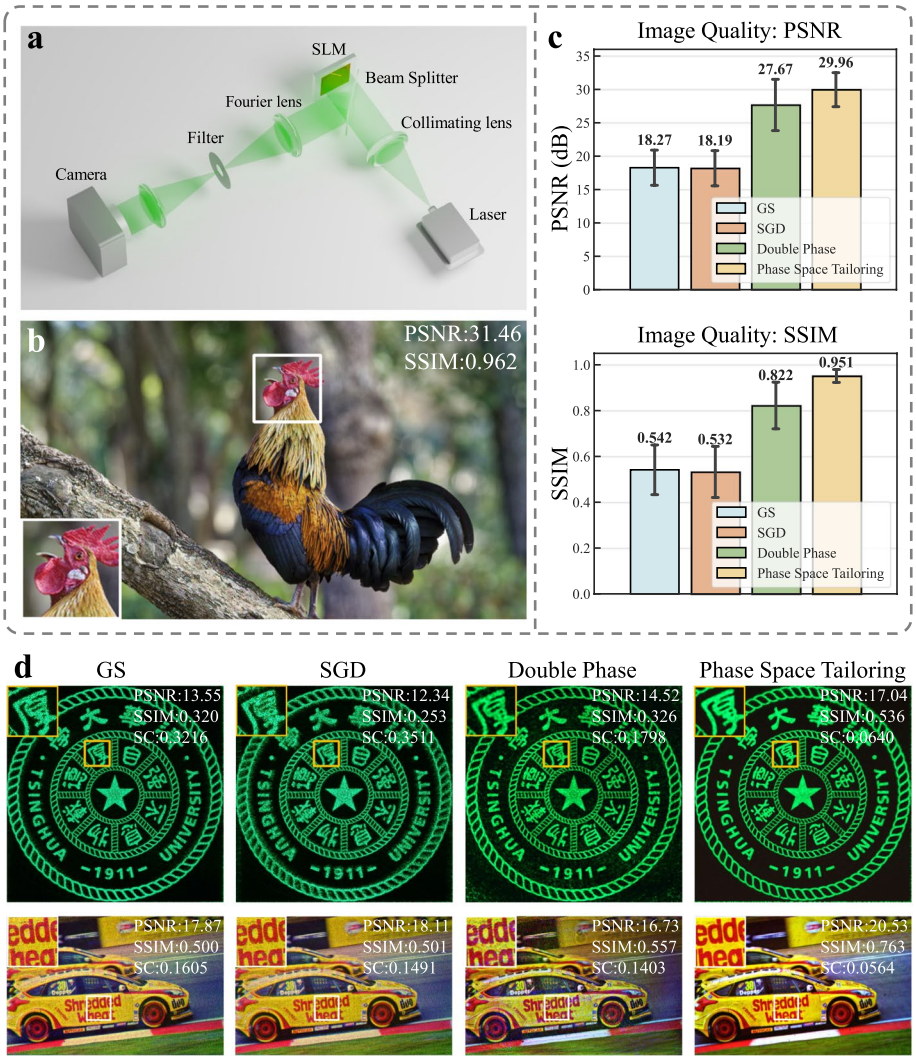

Fig. 3 Experimental results. **a** Schematic of optical experimental setup. The modulated light is filtered by a 4*f* system to achieve phase space tailoring, then propagating and captured by a camera. **b** Simulation result. **c** Quantitative comparisons using PSNR and SSIM for different methods. **d** Optical results, where the phase space tailoring method effectively suppresses the speckle noise and artifacts, and achieving the highest image quality. Additional monochrome results can be found in Sect. 2 J of the Supplementary Materials

The phase space tailoring method can reconstruct 3D scenes across a continuous and extensive depth range. Figure 4b showcases the optical reconstructions of a continuous 3D scene with a depth range spanning from 7.0 cm to 9.8 cm. Given the hardware parameters mentioned, the axial sampling criterion is 1 mm, then $d_z = 0.7$ mm is applied here. Details about the axial sampling criterion can be found in Table S1 of the Supplementary Materials. The images from the first to the last column focus on the nearest rock, the alarm clock, and the farthest pen, respectively. The phase space tailoring method achieves a high level of image quality, along with distinct defocus blur. It can be observed that when the focus is set at a specific depth, the scenes at other depths present noticeable defocus blur (Fig. 4b).

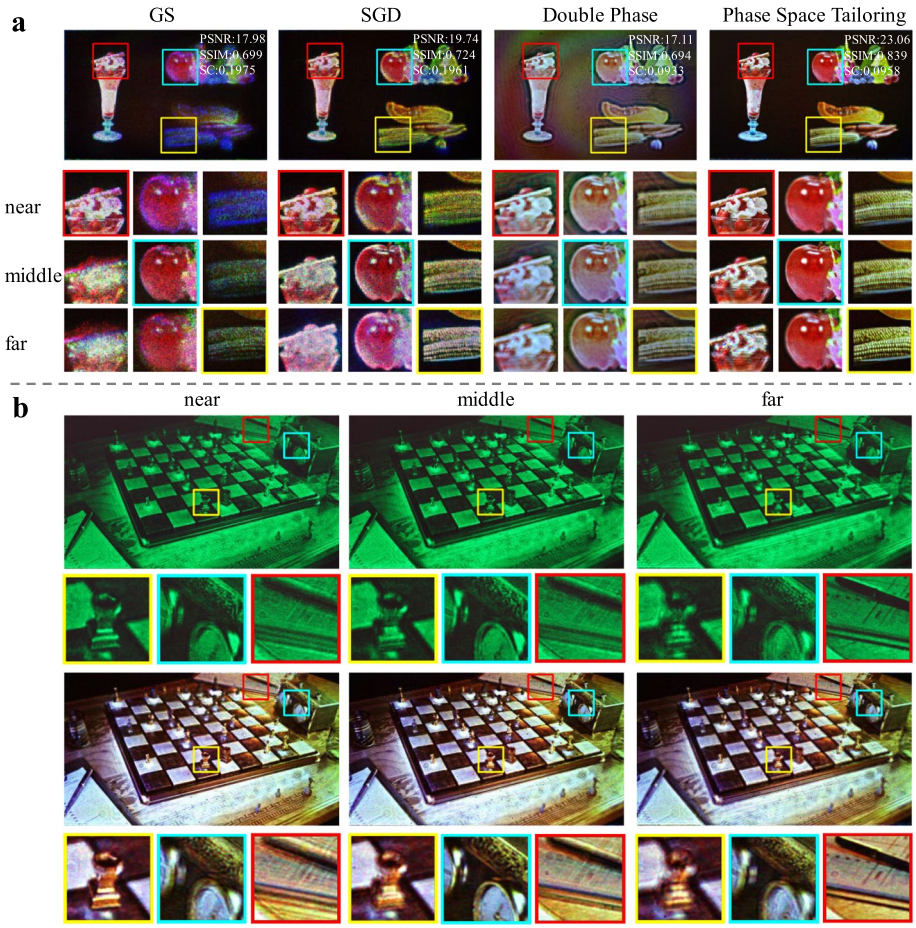

Fig. 4 3D experimental demonstration of the proposed method. **a** Optical reconstructions of three images placed at different depths. The three images are placed at 7.0 cm, 8.0 cm, and 9.0 cm, respectively. The optical reconstructions of the GS and SGD methods are accompanied with speckle noise, which becomes more severe at defocus regions. The double phase method produces background noise in this case and reduces the image contrast. The optical reconstructions of the phase space tailoring method are of highest image contrast and no speckle artifacts. **b** A 40-layers scene with $z_1 = 70$ mm and $d_z = 0.7$ mm

Discussion

To assess the impact of the proposed phase space tailoring method, all baselines are tested with the original ASM [14] and the proposed forward propagation model with phase space tailoring. In Fig. 5a, the first row displays the experimental results of the GS, SGD, double phase, and SGD method with the original ASM and the proposed loss function. The second row shows the experimental results of different methods using the proposed phase space tailoring propagation model for the same baselines. The enlarged parts on the upper left show that the proposed phase space tailoring method alone improves the image quality. Additionally, the proposed physics-informed loss function can further eliminate the speckle noise. However, when the phase space tailoring is combined with the GS method, the optical image quality remains subpar due to the unannihilated vortices. These isolated phase vortices interfere with each other, leading to unwanted rippling artifacts in the results. The proposed physics-informed loss function with the original ASM yields low quality results with poor image contrast. This would

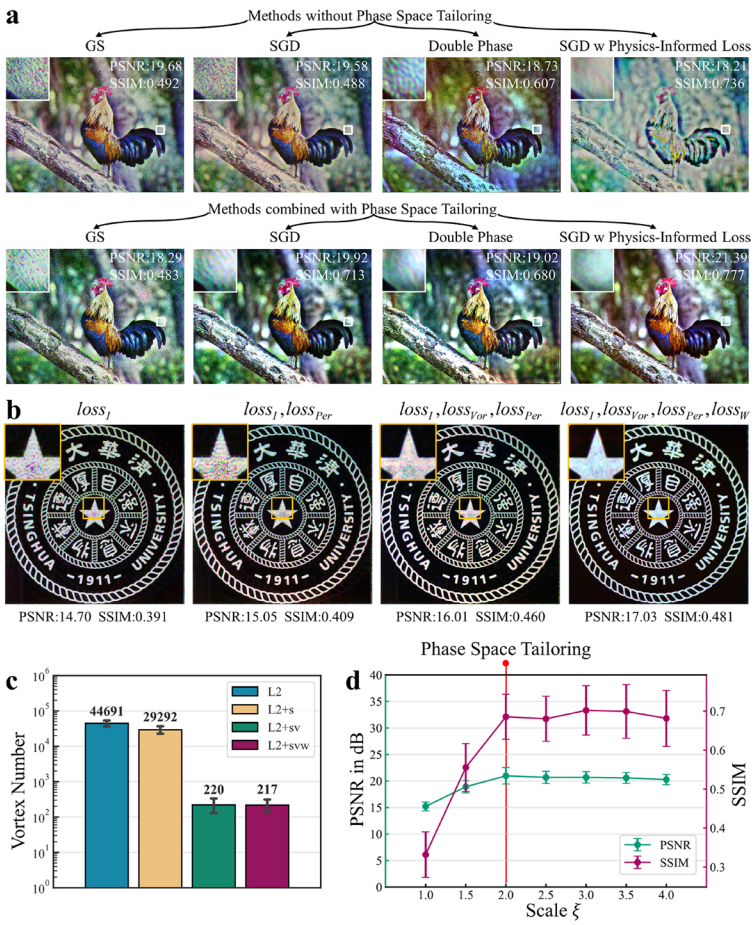

Fig. 5 Ablation study. **a** Apples-to-apples comparison that validates the contribution and efficacy of the proposed phase space tailoring wave propagation model. The first row is the experimental results with original ASM propagation. The second row is the experimental results with phase space tailoring. **b** Ablation study for different loss terms. **c** Quantitative comparison of the number of phase vortices for different loss terms. L2 is the mean square error. s, v, and w indicate the perceptual loss $loss_{Per}$, the vortex loss $loss_{Vor}$, and the weighted loss $loss_W$, respectively. **d** Image quality of the CITL method improves with a proper tailoring of phase space. The horizontal axis is the scale of tailoring. The left and right vertical axes are the mean PSNR and SSIM values of 12 tested images, the error bars are the standard deviations. The phase space tailoring point is indicated by a red vertical line

be attributed to the strong constraints imposed by the vortex regularized term. This experiment demonstrates that while the proposed phase space tailoring method effectively reduces the speckle noise on its own, the physics-informed loss function is highly dependent on the phase space tailoring wave propagation model and cannot function independently.

A detailed ablation study, qualitatively and quantitatively, shows the contributions of each loss term of Eq. 7 from standard $loss_I$ to proposed method, step by step. Optical experiments are used to assess the impact of the individual loss function terms on the overall improvement of the CGHs (Fig. 5b). It shows that the intensity constraint $loss_I$ and $loss_{Per}$ are not effective in eliminating phase vortices. The remaining phase vortices introduces the speckles in the optical reconstructions. The quantitative analysis is presented in Fig. 5c, where the number of remaining phase vortices in non-zero

regions of the image is counted for different loss terms. As a result, the proposed stochastic phase gradient approach, $loss_{Vor}$, is proved to be effective in eliminating the phase vortices (Fig. 5b, c). Moreover, the weighted constraint strategy, $loss_W$, improves both the uniformity and the contrast of the reconstructions. A more detailed comparison of the phase vortex elimination performance of different methods can be found in Sect. 2I of the Supplementary Materials.

The proposed phase space tailoring method can also be integrated to enhance the performance of the state-of-the-art CGH methods. Figure 5d illustrates the improvement achieved by applying the phase space tailoring method to the CITL approach. Typically, the diameter of the iris in CITL is selected empirically [54]. However, we demonstrate that the CITL can achieve optimal performance by using the iris diameter determined through the phase space tailoring (Eq. 6). In Fig. 5d, the iris diameter is $A_x = \lambda z/\xi d_x$ and different scales ξ are tested. When $\xi = 2$, the iris diameter A_x matches the diameter obtained from the phase space tailoring equation (Eq. 6). Beyond $\xi = 2$, increasing the scale does not significantly improve image quality (Fig. 5d); instead, it leads to blurred details due to a smaller iris diameter. Optical results can be found in Sect. 2B of the Supplementary Materials. Furthermore, the physical model is vital for the performance of learning-based CGH algorithms. We demonstrate that the proposed method can also be integrated into deep learning methods and achieve high-quality results. The training framework and optical results can be found in Sect. 2B of the Supplementary Materials.

Conclusion

In summary, we have presented a phase space tailoring framework for optimizing CGHs to achieve high-quality 2D and 3D optical reconstructions. The proposed method enables physically consistent discrete sampling across a continuous and large depth range by tailoring the phase space. Furthermore, when combined with the vortex regularization, our proposed method effectively eliminates the speckle noise and artifacts, resulting in full-color optical reconstructions with enhanced color fidelity. The feasibility of the phase space tailoring method for continuous and large-depth-range 3D optical reconstruction is validated with a 40-layer 3D scene.

While the proposed method outperforms others in terms of reconstruction accuracy, its runtime is not optimal. The computation speed can be further enhanced using a lower-level programming language and higher-performance computers. Moreover, this 3D CGH optimization framework with phase space tailoring can also be leveraged for training neural networks to enable real-time CGH synthesis. The proposed method has potential applications in various fields where optimizing the 3D diffraction fields is necessary, such as holographic display, optical manipulation, or laser fabrication.

Methods

Optical setup

All the experiments in this study were performed on our holographic display system, the setup shown in Fig. 3a is utilized. A FISBA READYBeam laser source with wavelengths

of 450 nm, 520 nm, and 638 nm is collimated and incident on the SLM, sequentially. A Meadowlark Optics 256 Gy-scale level reflective phase-only SLM with a resolution of 1920×1152 and a pixel pitch of 9.2 μm is used. The modulated laser beam from the SLM is filtered through a $4f$ system and then captured by a Canon 600D camera.

Details of optimization algorithm

In the implementation, the weights of the regularization terms are set as follows: $\lambda_{Vor}=0.5$, $\lambda_{Per}=0.05$, and $\lambda_{W}=0.5$. The dark region threshold a is 0.04, the learning rates for the hologram and scale parameter are 0.05 and 0.02, respectively. During optimization, a step learning rate decay scheduler is adopted with a decay rate of 0.8 per hundred iterations. For 3D CGH optimization, the distance from each layer to the hologram is rounded to be an integer multiple of the wavelength to avoid phase jumps between layers. Since the remainder is smaller than the wavelength, the rounding operation has a negligible influence on the reconstruction. The pseudocode of the proposed phase space tailoring method is outlined in Algorithm 1.

Algorithm 1 Phase space tailoring method

maxiter: maximum number of iterations
num_layer: number of layers for layer-based 3D CGH
φ_0: random initial phase uniformly distributed between −0.5 and 0.5
A: constant
s: a learnable scale parameter, initialize to 1
$gd\{loss;\varphi_k\}$: update the hologram φ_k with gradient decent
for k in 1... *maxiter* **do**
    $loss \leftarrow 0$
    for i in 1... *num_layer* **do**
        $loss \leftarrow +\left\| sM_i \left| P_{PST}^{(z_i)} \{A\exp(i\varphi_k)\} \right| - M_i T \right\|_2$
        $loss \leftarrow +\lambda_{per} loss_{per} \left\{ sM_i \left| P_{PST}^{(z_i)} \{A\exp(i\varphi_k)\} \right|, M_i T \right\}$
        $loss \leftarrow +\lambda_{Vor} loss_{Vor} \left\{ P_{PST}^{(z_i)} \{A\exp(i\varphi_k)\}, M_i \right\}$
        $loss \leftarrow +\lambda_{W} loss_{W} \left\{ s \left| P_{PST}^{(z_i)} \{A\exp(i\varphi_k)\} \right|, T \right\}$
    end for
    $\varphi_{k+1} \leftarrow gd\{loss;\varphi_k\}$
end for
Output: $\varphi_{maxiter}$

Vortex regularization

The phase vortex is a helically structured wavefront [55, 56] that diverges from a singularity point. The phase value at the singular point is indeterminate, which is the reason for the vanishing gradient and resulting in the iterative stagnation [49]. The closed line integral of the phase gradient around the vortex is an integer multiple of 2π:

$$\oint \nabla\Phi(O)dl = q2\pi, \tag{10}$$

where ∇ is the vector differential (Nabla) operator, $\Phi(O)$ represents the phase term of reconstructed complex amplitude O, and q is the topological charge. The phase gradient

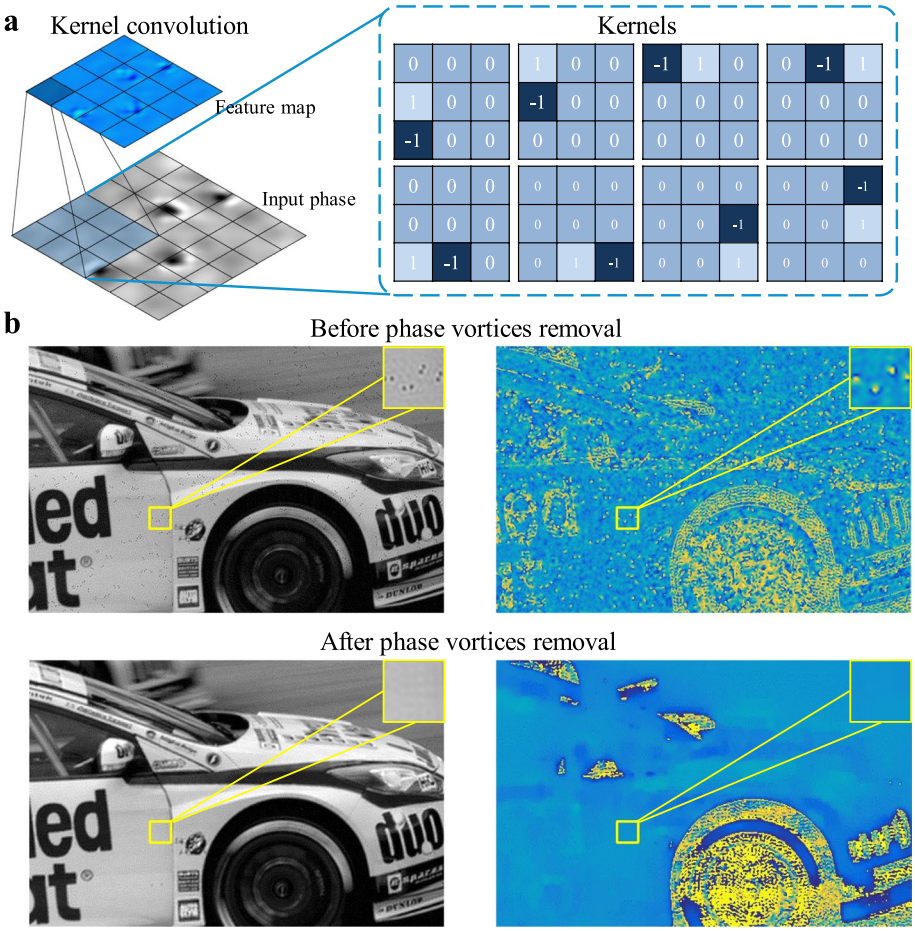

Fig. 6 The vortex annihilation. **a** Kernel convolution for phase gradient. **b** Reconstructed amplitude and phase with and without phase vortices removal. The speckle can be eliminated through the proposed method

kernels (Fig. 6a) can be used to detect the vortices. If the sum of all eight wrapped phase gradient distributions results in $q2\pi$ at a specific location, then there is a singularity point. The removal of phase vortices can be achieved by adding phase vortices with the opposite topological charge point by point. However, this procedure is time-consuming and impractical for high-resolution CGH optimization.

Here, a simplified vortex removal method called stochastic phase gradient regularization is adopted. The closed line integral in Eq. 10 can be expressed with 8 convolution kernels, as shown in Fig. 6a. Achieving the closed line integral requires a phase unwrapping operation, which unfortunately is non-differentiable. To address this issue, an approximation algorithm is adopted. During each iteration, we randomly exclude one kernel K_k from the eight available kernels and convolve the remain ones with the reconstructed phase. Then the vortex regularization term $loss_{Vor}$ is defined as:

$$loss_{Vor}\{O, M_i\} = \frac{1}{2}\left\| M_i\left(\sum_{j\neq k} K_j * m\Phi(O)\right)\right\|_1 + \frac{1}{2}\left\| M_i\left(\sum_{j\neq k} K_j * m\Phi(O)\right)\right\|_2. \quad (11)$$

In $loss_{Vor}$, * denotes convolution and K_j represent convolution kernels that produce the approximate phase gradient. For each iteration, K_k is randomly exclude from the eight kernels. With the stochastic phase gradient strategy, the issue of phase ambiguity and vanishing gradient at the phase vortices is avoided. In this way, the phase vortices can be efficiently eliminated without degrading the texture information (Fig. 6b). Detailed discussions about the proposed physics-informed loss function can be found in Sect. 2G of the Supplementary Materials.

Weighted constraint strategy

In this study, a weighted constraint strategy is adopted to expand the optimizing space. Specifically, as the phase vortices in zero-amplitude region would not cause the speckle noise, they are not considered in the vortex regularization. The weighted constraint is achieved through a binary mask m, as shown in Eq. 12. This mask indicates the nonzero region in target images, which is defined as:

$$m(x, y) = \begin{cases} 1 & \mathrm{T}(x, y) \geq a, \\ 0 & \text{otherwise.} \end{cases}, \quad (12)$$

where a is a threshold defining the dark region. The dark region is further constrained through an intensity regularization:

$$loss_W\{O, T\} = \|(1-m)|O| - (1-m)T\|_2. \quad (13)$$

In conclusion, the weighted constraint adopted is as follows:

$$loss_{weight} = \begin{cases} loss_{Vor} & O(x, y) \in m, \\ loss_W & \text{otherwise.} \end{cases}. \quad (14)$$

Abbreviations

3D	Three-dimensional
2D	Two-dimensional
CGH	Computer-generated holography
SLM	Spatial light modulator
SBP	Space-bandwidth product
GS	Gerchberg-Saxton method
CITL	Camera-in-the-loop method
SGD	Stochastic gradient descent method
NOVO-CGH	Non-Convex Optimization for VOlumetric CGH
ASM	Angular spectrum method
WDF	Wigner distribution function
PSD	Phase space diagram
PSNR	Peak signal-to-noise ratio
SSIM	Structural similarity index measure
SC	Speckle contrast

Supplementary Information

The online version contains supplementary material available at https://doi.org/10.1186/s43074-024-00149-0.

Supplementary Material 1.

Acknowledgements
Not applicable.

Authors' contributions
R. Zhu, L. Chen, and H. Zhang designed and conducted the experiments and programmed the algorithm. J. Xiao contributed to the experiments and the conducted data analyses. R. Zhu, L. Chen, and H. Zhang wrote the manuscript.

Funding
National Natural Science Foundation of China (NSFC) 62035003. National Key Research and Development Program of China No.2021YFB2802100.

Availability of data and materials
The data that support the findings of this study are available from the corresponding author upon reasonable request.

Declarations

Competing interests
The authors declare no competing interests.

Received: 27 May 2024 Revised: 22 September 2024 Accepted: 29 September 2024
Published online: 22 October 2024

References

1. Campbell M, Sharp DN, Harrison MT, Denning RG, Turberfield AJ. Fabrication of photonic crystals for the visible spectrum by holographic lithography. Nature. 2000;404(6773):53–6.
2. Pégard NC, Mardinly AR, Oldenburg IA, Sridharan S, Waller L, Adesnik H. Three-dimensional scanless holographic optogenetics with temporal focusing (3D-SHOT). Nat Commun. 2017;8(1):1228.
3. Reutsky-Gefen I, Golan L, Farah N, Schejter A, Tsur L, Brosh I, et al. Holographic optogenetic stimulation of patterned neuronal activity for vision restoration. Nat Commun. 2013;4(1):1509.
4. Curtis JE, Koss BA, Grier DG. Dynamic holographic optical tweezers. Opt Commun. 2002;207(1–6):169–75.
5. Di Leonardo R, Ianni F, Ruocco G. Computer generation of optimal holograms for optical trap arrays. Opt Express. 2007;15(4): 1913.
6. Chang C, Bang K, Wetzstein G, Lee B, Gao L. Toward the next-generation VR/AR optics: a review of holographic near-eye displays from a human-centric perspective. Optica. 2020;7(11):1563–78.
7. Yu H, Lee K, Park J, Park Y. Ultrahigh-definition dynamic 3D holographic display by active control of volume speckle fields. Nat Photonics. 2017;11(3):186–92.
8. Pi D, Liu J, Wang Y. Review of computer-generated hologram algorithms for color dynamic holographic three-dimensional display. Light Sci Appl. 2022;11(1):231.
9. Zhan T, Xiong J, Zou J, Wu S-T. Multifocal displays: review and prospect. PhotoniX. 2020;1(1):10.
10. Xiong J, Zhong H, Cheng D, Wu S-T, Wang Y. Full degree-of-freedom polarization hologram by freeform exposure and inkjet printing. PhotoniX. 2023;4(1):35.
11. Wang D, Li Y-L, Chu F, Li N-N, Li Z-S, Lee S-D, et al. Color liquid crystal grating based color holographic 3D display system with large viewing angle. Light Sci Appl. 2024;13(1):16.
12. Lesem LB, Hirsch PM, Jordan JA. The kinoform: a new wavefront reconstruction device. IBM J Res Dev. 1969;13(2):150–5.
13. Shimobaba T, Kakue T, Real-time IT, low speckle holographic projection. IEEE 13th Int. Conf. Ind. Inform. INDIN, Cambridge, United Kingdom: IEEE. Cambridge. 2015;2015:732–41.
14. Zhang H, Cao L, Jin G. Computer-generated hologram with occlusion effect using layer-based processing. Appl Opt. 2017;56(13):F138–43.
15. Shimobaba T, Kakue T, Ito T. Review of fast algorithms and hardware implementations on computer holography. IEEE Trans Ind Inform. 2016;12(4):1611–22.
16. Zhang H, Zhao Y, Cao L, Jin G. Layered holographic stereogram based on inverse Fresnel diffraction. Appl Opt. 2016;55(3):A154–9.
17. Hsueh CK, Sawchuk AA. Computer-generated double-phase holograms. Appl Opt. 1978;17(24):3874–83.
18. Qi Y, Chang C, Xia J. Speckleless holographic display by complex modulation based on double-phase method. Opt Express. 2016;24(26):30368–78.
19. Maimone A, Georgiou A, Kollin JS. Holographic near-eye displays for virtual and augmented reality. ACM Trans Graph. 2017;36(4):1–16.
20. Shi L, Li B, Kim C, Kellnhofer P, Matusik W. Towards real-time photorealistic 3D holography with deep neural networks. Nature. 2021;591(7849):234–9.
21. Gerchberg RW. A practical algorithm for the determination of phase from image and diffraction plane pictures. Optik. 1972;35:237–46.

22. Fienup JR. Phase retrieval algorithms: a comparison. Appl Opt. 1982;21(15): 2758.
23. Peng Y, Dun X, Sun Q, Heidrich W. Mix-and-match holography. ACM Trans Graph. 2017;36(6):191–201.
24. Matsushima K, Shimobaba T. Band-limited angular spectrum method for numerical simulation of free-space propagation in far and near fields. Optics Express. 2009;12:19662–73.
25. Chen L, Tian S, Zhang H, Cao L, Jin G. Phase hologram optimization with bandwidth constraint strategy for speckle-free optical reconstruction. Opt Express. 2021;29(8):11645–63.
26. Madsen AEG, Eriksen RL, Glückstad J. Comparison of state-of-the-art Computer Generated Holography algorithms and a machine learning approach. Opt Commun. 2022;505: 127590.
27. Peng Y, Choi S, Padmanaban N, Wetzstein G. Neural holography with camera-in-the-loop training. ACM Trans Graph. 2020;39(6):185.
28. Chen C, Kim D, Yoo D, Lee B, Lee B. Off-axis camera-in-the-loop optimization with noise reduction strategy for high-quality hologram generation. Opt Lett. 2022;47(4):790–3.
29. Zhang J, Pégard N, Zhong J, Adesnik H, Waller L. 3D computer-generated holography by non-convex optimization. Optica. 2017;4(10):1306–13.
30. Chen C, Lee B, Li N-N, Chae M, Wang D, Wang Q-H, et al. Multi-depth hologram generation using stochastic gradient descent algorithm with complex loss function. Opt Express. 2021;29(10):15089–103.
31. Makey G, Yavuz Ö, Kesim DK, Turnalı A, Elahi P, Ilday S, et al. Breaking crosstalk limits to dynamic holography using orthogonality of high-dimensional random vectors. Nat Photonics. 2019;13(4):251–6.
32. Choi S, Gopakumar M, Peng Y, Kim J, Wetzstein G. Neural 3D holography: learning accurate wave propagation models for 3D holographic virtual and augmented reality displays. ACM Trans Graph. 2021;40(6):240.
33. Gopakumar M, Lee G-Y, Choi S, Chao B, Peng Y, Kim J, et al. Full-colour 3D holographic augmented-reality displays with metasurface waveguides. Nature. 2024;629(8013):791–7.
34. Choi S, Gopakumar M, Peng Y, Kim J, O'Toole M, Wetzstein G. Time-multiplexed neural holography: a flexible framework for holographic near-eye displays with fast heavily-quantized spatial light modulators. ACM SIGGRAPH 2022 Conf. Proc., 2022, p. 1–9.
35. Lee B, Kim D, Lee S, Chen C, Lee B. High-contrast, speckle-free, true 3D holography via binary CGH optimization. Sci Rep. 2022;12(1):2811.
36. Liu S-B, Xie B-K, Yuan R-Y, Zhang M-X, Xu J-C, Li L, et al. Deep learning enables parallel camera with enhanced- resolution and computational zoom imaging. PhotoniX. 2023;4(1):17.
37. Zhang Y, Wang Y, Wang M, Guo Y, Li X, Chen Y, et al. Multi-focus light-field microscopy for high-speed large-volume imaging. PhotoniX. 2022;3(1):30.
38. Wang D, Li Z-S, Zheng Y, Zhao Y-R, Liu C, Xu J-B, et al. Liquid lens based holographic camera for real 3D scene hologram acquisition using end-to-end physical model-driven network. Light Sci Appl. 2024;13(1):62.
39. Shi L, Li B, Matusik W. End-to-end learning of 3D phase-only holograms for holographic display. Light Sci Appl. 2022;11(1):247.
40. Liu K, Wu J, He Z, Cao L. State key laboratory of precision measurement technology and instruments, department of precision instruments, Tsinghua University, Beijing 100084, China. 4K-DMDNet: diffraction model-driven network for 4K computer-generated holography. Opto-Electron Adv. 2023;6(5):220135.
41. Alonso MA. Wigner functions in optics: describing beams as ray bundles and pulses as particle ensembles. Adv Opt Photonics. 2011;3(4):272–365.
42. Xiao J, Zhang W, Zhang H. Sampling analysis for Fresnel diffraction fields based on phase space representation. J Opt Soc Am A. 2022;39(2):A15-28.
43. Zhang W, Zhang H, Sheppard CJR, Jin G. Analysis of numerical diffraction calculation methods: from the perspective of phase space optics and the sampling theorem. J Opt Soc Am A. 2020;37(11):1748–66.
44. Zhang H, Xiao J, Chen L, Zhu R. Computer Holography Based on Phase Space Analysis. Digit. Hologr. Three-Dimens. Imaging 2022, Optica Publishing Group, Cambridge; 2022, p. M6A.5.
45. Wigner E. On the quantum correction for thermodynamic equilibrium. Phys Rev. 1932;40(5):749–59.
46. Bastiaans MJ. Wigner distribution function and its application to first-order optics. J Opt Soc Am. 1979;69(12):1710–6.
47. Wyrowski F, Bryngdahl O. Iterative Fourier-transform algorithm applied to computer holography. J Opt Soc Am A. 1988;5(7):1058–65.
48. Senthilkumaran P, Wyrowski F. Phase synthesis in wave-optical engineering: mapping- and diffuser-type approaches. J Mod Opt. 2002;49(11):1831–50.
49. Senthilkumaran P, Wyrowski F, Schimmel H. Vortex Stagnation problem in iterative Fourier transform algorithms. Opt Lasers Eng. 2005;43(1):43–56.
50. Chen L, Zhang H, He Z, Wang X, Cao L, Jin G. Weighted Constraint Iterative Algorithm for Phase Hologram Generation. Appl Sci. 2020;10(10): 3652.
51. Zhao Y, Cao L, Zhang H, Kong D, Jin G. Accurate calculation of computer-generated holograms using angular-spectrum layer-oriented method. Opt Express. 2015;23(20):25440–9.
52. Agustsson E, Timofte RNTIRE. Challenge on Single Image Super-Resolution: Dataset and Study. 2017 IEEE Conf. Comput. Vis. Pattern Recognit. Workshop CVPRW, Honolulu, HI, USA: IEEE. Honolulu. 2017;2017:1122–31.
53. Lee S, Kim D, Nam S-W, Lee B, Cho J, Lee B. Light source optimization for partially coherent holographic displays with consideration of speckle contrast, resolution, and depth of field. Sci Rep. 2020;10(1):18832.
54. Chen L, Zhu R, Zhang H. Speckle-free compact holographic near-eye display using camera-in-the-loop optimization with phase constraint. Opt Express. 2022;30(26):46649.
55. Basistiy IV, Soskin MS, Vasnetsov MV. Optical wavefront dislocations and their properties. Opt Commun. 1995;119(5–6):604–12.
56. Nye JF, Berry MV. Dislocations in wave trains. Proc R Soc Lond Math Phys Sci. 1974;336(1605):165–90.

Publisher's Note